THESIS FOR THE DEGREE OF LICENTIATE OF ENGINEERING

IN THERMO AND FLUID DYNAMICS

Measurements and Prediction of Friction Drag of Rough Surfaces

BERCELAY NIEBLES ATENCIO

Measurements and Prediction of Friction Drag of Rough Surfaces

BERCELAY NIEBLES ATENCIO

Department of Applied Mechanics
Chalmers University of Technology
SE-412 96 Gothenburg
Sweden
Telephone +46 (0)31 772 1000

Measurements and Prediction of Friction Drag of Rough Surfaces

Thesis for the degree of Licentiate of Engineering in Thermo and Fluid Dynamics
BERCELAY NIEBLES ATENCIO
Department of Applied Mechanics
Division of Fluid Dynamics
Chalmers University of Technology

ABSTRACT

Owing to the increased sea transportation of goods, the environmental impacts of this activity are becoming more and more important, since a ship experiences resistance that directly affects its performance and fuel consumption.

The growth of marine organisms (fouling) on ship hulls increases the roughness of the hull surface, which in turn causes a rise in ship resistance with a consequent increase in fuel consumption and greenhouse emissions of up to 40%.

Antifouling coatings have been developed and used to counteract the effect of fouling on ships and boats, but a desirable characteristic of a good antifouling coating is of course a low contribution to drag. The immediate effect of an antifouling on a hull is to increase its roughness. Its effect on vessel resistance has been studied by some researchers, but there is no common agreement on the way the drag should be characterized, which implies finding the velocity decrement or roughness function, ΔU^+.

This thesis examines different approaches to characterizing the drag caused by antifouling paints. One of the approaches implies submicron resolution boundary layer measurements with Particle Image Velocimetry (PIV), which, to the best of our knowledge, has not been tried before. Characterization from torque measurements on rotating disks was also evaluated together with drag measurements on towed flat plates. These data have been used to validate resolved CFD simulations, and the outcome is a promising method for characterizing the drag of any arbitrary rough surface.

Keywords: Hydrodynamics, Turbulent Boundary Layers, Roughness Function, PIV, Rotating Disk, Flat Plate, Resolved CFD, RANS, Wall Functions.

I

ACKNOWLEDGEMENTS

LIST OF PUBLICATIONS

This thesis is based on the work contained in the following publications (appended papers):

1. Niebles Atencio B., Tokarev M., Chernoray V., (2016). "Submicron Resolution Long-Distance Micro-PIV Measurements in a Rough-Wall Boundary Layer" 18th International Symposium on the Application of Laser and Imaging Techniques to Fluid Mechanics, Lisbon.
2. Niebles Atencio B., Chernoray V., (2016). "A Resolved CFD Approach for Drag Characterization of Antifouling Paints". Manuscript in preparation for publication.

TABLE OF CONTENTS

1.   INTRODUCTION

1.1   Background

Transportation is a necessity for worldwide business activities. In 2014, almost 10 billion tons of goods were loaded and transported by sea and studies indicate that the volume of seaborne shipment has expanded 3.4% (UNCTAD, 2015). Because of this greater transportation of goods, the environmental impacts of this activity are becoming increasingly important.

An emerging problem is to protect the hull of ships from the growth of a vast range of marine organisms (fouling), because a hull surface that has become rough due to the growth of algae, bacteria and barnacles may increase the ship's resistance up to 40% (Taylan, 2010) and consequently increase fuel consumption and greenhouse gas emissions. Therefore, there is a desire in the naval architecture field to gain a full understanding of the effect of roughness. At present, a roughness allowance is calculated and added to frictional and residual coefficients when determining the overall drag of a full scale ship (ITTC, 1978). Towsin et al. (1981) wanted to predict the roughness penalty more accurately and came up with a formulation based on the mean hull roughness and the Reynolds number, but representing the mean roughness over the hull of ships and boats is quite challenging. As is well known, two of the major contributors to the surface roughness of a ship are the hull coating and fouling. Antifouling coatings have been developed and used to counteract the effect of fouling on ships and boats, but a desirable characteristic of a good antifouling coating is of course a low contribution to drag. Many researchers (e.g. Candries & Atlar, 2003) have studied the effect of antifouling coatings on the vessel drag but there is no common agreement on this topic.

Despite efforts to understand the roughness effect on drag over marine structures, the lack of further studies and methods to accurately determine the texture characteristics of rough surfaces led the ITTC Specialist Committee on Powering Performance Prediction to conclude that there are reasons for questioning the accuracy of the currently used methods (ITTC, 2005). With this in mind, Flack and Schultz (2010) proposed a method to obtain equivalent sand-grain roughness height based on the root mean square of the roughness height and the skewness of the roughness probability density function. This would enable determination of the frictional drag coefficient.

Characterizing the drag of a rough surface implies finding the velocity decrement caused by the frictional drag of the surface as a function of the roughness Reynolds number. This relationship is commonly known as a roughness function (Clauser, 1954 and Hama, 1954) and is unique for any particular surface roughness geometry. Once the roughness function for a given rough surface is known, it can be used in a numerical analysis to predict the drag of any body covered with that roughness.

The present study shows some indirect methods revised and used to validate a newly developed approach based on resolved RANS simulations to evaluate the drag of antifouling paints. The new CFD based approach can be useful to replace expensive experiments for finding the roughness function. To start with, a review is given of current approaches for obtaining the roughness function and the indirect methods. Further, an approach for obtaining the roughness function for antifouling paints from resolved RANS simulations is described and the results are validated by experimental data from rotating disk and towing tank methods. Finally, the validity of the roughness function is checked by implementing it in wall-function based RANS simulations.

1.2   Methods used in Fluid Dynamics

Almost a century ago, Nikuradse (1933) carried out one of the most famous investigations of the effect of wall roughness on turbulent flows using pipes with uniform sand coating and different sizes. In this case of homogeneous sand, the roughness effect on the boundary layer depended only on the average sand-grain height k_s. His work was extended by Colebrook (1939), who analyzed the flow in commercial pipes, and by Moody (1944), who related the pressure drop in a pipe to the relative roughness (ratio of roughness height to pipe diameter) and Reynolds number. He consolidated the results into a very useful diagram commonly employed as an engineering tool. Results reported by Allen et al. (2005) show that the pressure drop in the Moody diagram is overestimated in transitionally rough regimes for honed and commercial steel pipes. This clearly indicates that the Colebrook roughness function used in the formulation of the Moody diagram may not be applicable to a wide range of roughnesses of engineering interest, according to Flack & Schultz (2010).

One of the big questions is whether the condition of the surface has any effect on the turbulent boundary layer mean flow and turbulence structure. Clauser (1954) and Hama (1954) introduced the roughness function concept. They found that the effect of surface roughness on the mean flow was limited to the inner layer, causing a downward shift in the log-law called the roughness function, ΔU^+.

Raupach, Antonia & Rajagopalan (1991) concluded that there is strong experimental support of outer layer similarity in the turbulence structure over smooth and rough walls with regular roughness. This is termed the 'wall similarity' hypothesis, and it states that, at sufficiently high Reynolds number, turbulent structures are independent of wall roughness and viscosity outside the roughness sublayer (or viscous sublayer in the case of a smooth wall), the roughness sublayer being the region directly above the roughness, extending about $5\,k$ from the wall (where k is the roughness height) in which the turbulent motions are directly influenced by the roughness length scales. Moreover, experimental studies of Kunkel & Marusic (2006) and Flack, Schultz & Shapiro (2005) also provided support for wall similarity in smooth-wall and rough-wall boundary layers in terms of both the mean flow and the Reynolds stresses.

Jiménez (2004) stated that the conflicting views regarding the validity of the wall similarity hypothesis may be due to the effect of the relative roughness, k/δ, on the flow (where δ is the boundary layer thickness). Jiménez concluded that, if the roughness height is small compared to the boundary layer thickness ($k/\delta < 1/40$), the effect of the roughness should be confined to the inner layer and wall similarity will hold. If, on the other hand, the roughness height is large compared to the boundary layer thickness ($k/\delta > 1/40$), roughness effects on the turbulence may extend across the entire boundary layer, and the concept of wall similarity will be invalid. Jimenez also notes that the classical notion of wall similarity has implications far beyond roughness studies, extending to the fundamental concepts of turbulence modeling. For example, the basis of large eddy simulation (LES) is that the small turbulence scales have little influence on the large energy-containing scales. If surface roughness exerts an influence across the entire boundary layer, this may not be a valid assumption. Krogstad and Efros (2012) performed experiments with squared bars and circular rods as roughness elements and found that the scale ratio proposed by Jimenez should be higher for the wall similarity hypothesis to hold.

Some researchers show their attempts using computational fluid dynamics to understand the effect of roughness on the turbulent structures and statistics in the turbulent boundary layers. Numerical simulations of turbulent channel flow by Leonardi et al. (2003) show a roughness

effect in the outer layer. Ashrafian et al. (2004) performed DNS simulations of turbulent flow in a rod-roughened channel and found significant differences in the turbulence field between smooth and rough wall boundary layers. Bhaganagar et al. (2004) concluded (using a 3D "egg carton" pattern roughness) that the streamwise and spanwise dimensions of roughness elements of fixed height play a crucial role in determining whether the roughness affects the outer layer. Another paper reporting DNS studies on 3D and 2D roughness was presented by Lee et al. (2011), who corroborated that the wall similarity did not hold in the outer layer. However, in his paper, a possible explanation for a failed wall similarity case could be related to the arrangement of the roughness elements.

It is worth noting that numerical and experimental studies of roughness effects and the determination of roughness function have usually been conducted on regular and uniform distribution of roughness elements and shapes, as mentioned by Yuan & Piomelli (2014), who made LES simulations to determine the roughness function and equivalent sand-grain roughness height of realistic roughness replicated from hydraulic turbines. They found that k_s depends strongly on the topography of the surface and moments of surface height statistics, not predicting the roughness function as well as the predictions of the correlations based on slope parameters. This method is however very computationally expensive and we propose a new approach in this report.

1.3   Aim and Scope

The primary objective of this work is to establish reliable, but at the same time low resource consuming, methods with the aim of evaluating the drag resistance caused by arbitrary rough surfaces resulting from applying antifouling paints. The idea is to use CFD simulation supported by laboratory tests. The performance of resolved CFD will be examined for obtaining the roughness function and equivalent sand roughness of coatings with different roughness shapes.

A small scale rig has been designed and built in order to perform tests to determine the frictional resistance of coatings. Experiments carried out in the small scale rig were based on techniques such as Particle Image Velocimetry (PIV) and torque measurements. Flat plate data provided by an external participant in the project is also examined and used to provide additional support to the resolved CFD simulations.

2 THEORY

2.1 Surface Condition of a Ship Hull

The condition of the surface plays an important role in the magnitude of frictional resistance. The frictional resistance is induced by the frictional forces around the hull surface of a ship. There are two types of roughness that can be defined as permanent or physical and temporary or biological roughness.

Fig 1. Heavily fouled ship hull (source: http://www.european-coatings.com)

Any kinds of discontinuities and protruding parts that affect flow pattern over the hull surface fall within the category of permanent roughness. Examples are the shell plating deformations, welding seams, mounted cathodic protection, bilge keels etc. Unlike permanent roughness, the temporary roughness is mostly caused by fouling and can be controlled tangibly by viable means. The effect of this type of roughness depends on the average roughness of the underwater outer surface of the ship's hull.

The growth of marine organisms on marine structures is defined as fouling. It is known that fouling significantly increases frictional resistance, which accounts for approximately 70-90% of the total resistance of a ship, affecting the fuel consumption as well. Although it is not easy to determine the amount of increase in resistance, some studies showed that up to a 40% increase in a ship's resistance may be expected due to fouling (Taylan, 2010). It is estimated that more than 2500 species exist in the world that can cause fouling (Anderson et al. 2003). The amount of fouling greatly depends on the geographical regions in which fouling organisms live. These foulers can be classified into two categories, as micro and macro organisms. Slime or algae is an example of microfouling organisms that gives rise to resistance of about 1-2%. Hard-shelled fouling species such as barnacles, tube worms, mussels etc., on the other hand, may increase ship resistance by up to 40% if it is not controlled. Hard-shelled barnacles most often induce corrosion by damaging the paint system on which they attach.

2.2 Roughness function

Surface roughness is a defining feature of many of the high Reynolds-numbers flows found in engineering.

The effect of the surface roughness on the fluid is a decrease in the momentum in the log-law region (NB: in a wall-scaling and in a wall reference frame), which is clearly seen by a downshift in the velocity profile in the log law layer. This effect is a consequence of the increase in the frictional drag of the surface.

The classical log-law of the mean velocity profile in the inner part of a turbulent boundary layer can be expressed as:

$$U^+ = \frac{1}{\kappa} \ln(y^+) + B \tag{1}$$

Where U^+ is the inner boundary layer velocity, κ is the von Kármán constant (a value of $\kappa = 0.41$ is normally used), y^+ is the normalized distance from wall and B is the smooth-wall log-law intercept.
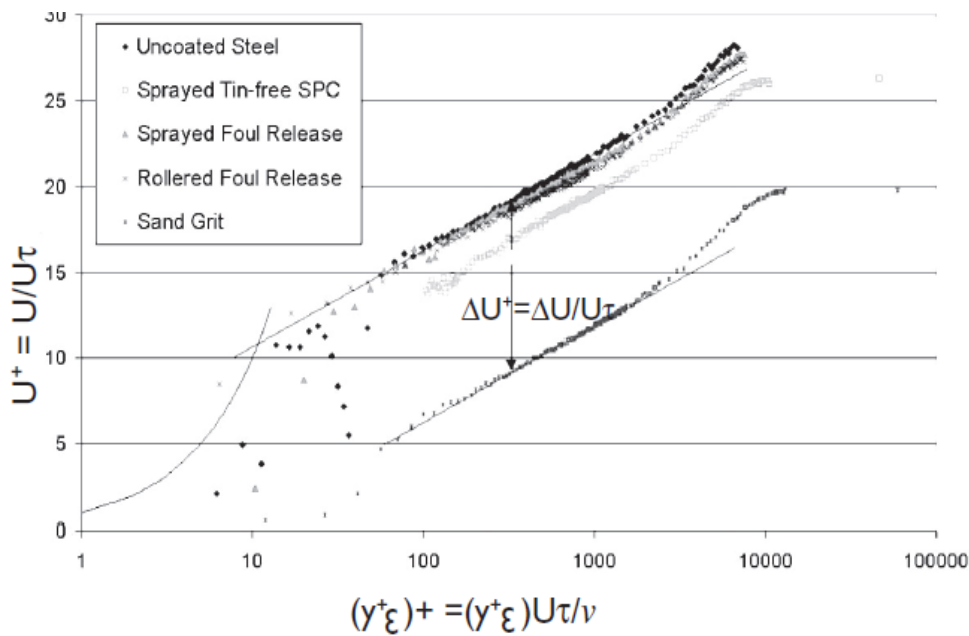

Fig. 2 Boundary layer velocity profiles in inner coordinates for different surface roughness and the downshift due to the roughness function, ΔU^+ (from Candries and Atlar, 2003)

In the case of rough surfaces, this law is also true but exhibits a downward shift called the roughness function, ΔU^+ (Fig. 2). The log law for rough walls would then be:

$$U^+ = \frac{1}{\kappa} \ln(y^+) + B - \Delta U^+ \tag{2}$$

ΔU^+ depends on roughness Reynolds number k^+ defined as the ratio of the roughness length scale k to the viscous length scale $\frac{\nu}{U_\tau}$, (ν is kinematic viscosity and U_τ is the friction velocity). It is customary to define roughness in terms of the equivalent sand-grain roughness k_s, and the Reynolds number based on the equivalent sand-grain roughness would then be:

$$k_s^+ = \frac{k_s \, U_\tau}{\nu} \tag{3}$$

A key step to determine the surface scales responsible for momentum deficit is the mapping of the roughness function over a range of roughness Reynolds numbers, k_s^+, taking into account the following considerations (Schlichting, 1979a):
- For small k_s^+, perturbations by roughness are damped out completely by fluid viscosity. This case is known as flow hydraulically smooth ($k_s^+ < 5$).
- As roughness increases, viscosity no longer damps out the eddies. Form and viscous drag contribute to the overall skin friction. This corresponds to the transitionally rough regime, where $5 < k_s^+ < 70$.
- As roughness increases further, skin friction is independent of the Reynolds number and the form drag of roughness is the dominant mechanism. This fully rough regime corresponds to the cases where $k_s^+ > 70$.

Hama (1954) showed that, knowing the definition of U_τ and c_f, one can express the smooth wall logarithmic law as:

$$\sqrt{\frac{2}{c_f}} = \frac{1}{\kappa} \ln(y^+) + B \tag{4}$$

The same can be done for the log law for rough walls:

$$\sqrt{\frac{2}{c_f}} = \frac{1}{\kappa} \ln(y^+) + B - \Delta U^+ \tag{5}$$

If we subtract the resulting expressions, one finds the roughness function ΔU^+ expressed as:

$$\Delta U^+ = \sqrt{\frac{2}{c_{fs}}} - \sqrt{\frac{2}{c_{fr}}} \tag{6}$$

This relation directly indicates the importance of parameter ΔU^+ and eliminates the need of velocity profiles to find the velocity defect due to roughness.

2.3   Rotating Disk Flow

The boundary layer that is formed on the disk surface is three-dimensional owing to a cross-flow velocity component, which is also denoted a radial velocity. Schlichting (1979b) explains that, due to friction, the fluid that is adjacent to the disk is carried by it and that the centrifugal acceleration then forces the fluid outwards, creating radial and tangential components (V_r and $V_\emptyset$ in Fig. 3). The mass of fluid that has been driven outwards by the action of the centrifugal force is replaced by an axial flow with velocity V_z.

The Reynolds number is given by

$$Re_r = V \frac{r}{\nu} \tag{7}$$

where r denotes the disk radius and $V = \omega r$ is the velocity at the tip of the disk, with ω as the angular velocity.

Another important dimensionless parameter is the moment or torque coefficient C_m, which is defined by Granville (1982) as

$$C_m = \frac{4M}{\rho r^5 (\phi \omega)^2} \qquad (8)$$

where M is the torque on one side of the disk and ϕ (defined as $\phi^2 = C_{m,en}/C_{m,\infty}$) is a swirl factor (normal values, $0 < \phi < 1$) that accounts for the swirl that may develop in enclosed rotating disk flows, reducing the effective angular velocity.
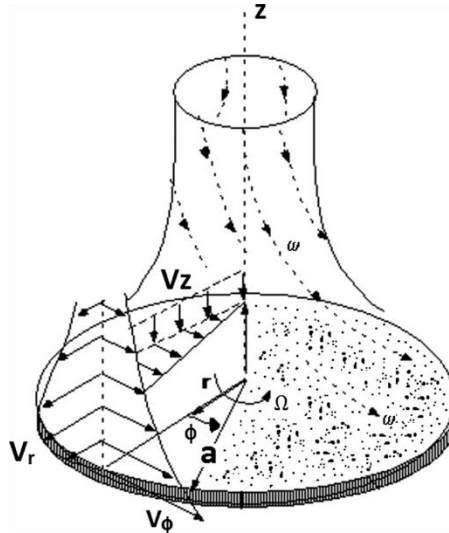

Fig. 3 Flow on rotating disks (source: https:// heattransfer.asmedigitalcollection.asme.org)

2.4   Particle Image Velocimetry (PIV)

Particle Image Velocimetry (PIV) indirectly measures flow velocity, see Raffel et al. (2007). The displacement of particles immersed in fluid flow is recorded photographically and analyzed. The PIV method is non-intrusive and allows recording of the flow velocity without disturbing the flow. At least two consecutive images, with known time interval are required in order to determine the displacement of the particles. The velocity can be then calculated by computing the displacement of the particles over the given time interval.

The displacement is derived from analyzing the intensity of the image pair using statistics based on specific areas of the image called interrogation windows. The particles used in PIV are called tracers and are critical in the PIV measurement since the fluid velocity is measured via the particle velocity. The first consideration when choosing the seeding particles is therefore visibility. The particles have to have a sufficient size and a good refractive index in order to achieve good scattering intensity. The size of the particles must be balanced with the fidelity of the particles following the flow. For acceptable tracing accuracy, the particle response time should be faster than the smallest time scale of the flow. The accuracy of the PIV measurement is therefore limited by the ability of the tracer particles to follow the fluid flow.

In order to find the particles' displacement over a short period of time, two images that have been successively recorded are compared. A small sub-area of the first image (interrogation window), is compared with the second image interrogation window by using a cross-correlation technique, resulting in a velocity vector for that particular particle pattern. This evaluation

process is repeated for all interrogation windows of the pair of images and the final outcome is a complete vector diagram of the flow under study (Fig. 4).
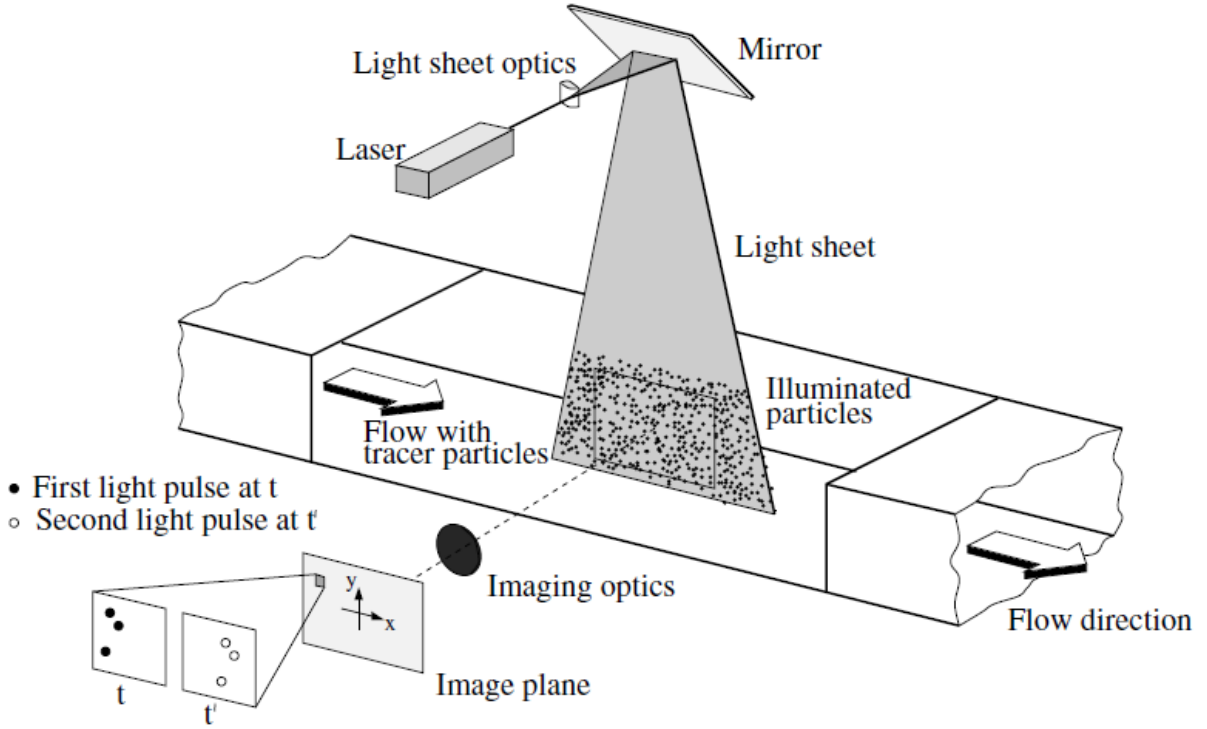

Fig. 4 Experimental arrangement for particle image velocimetry (from Raffel et al, 2007)

2.5   Turbulence Modeling

Turbulence modeling is to construct and use a turbulence model to predict turbulence and its effects. Turbulence is a phenomenon which is unsteady, viscous and three-dimensional. The disturbances responsible of creating turbulence can be thought of a series of three-dimensional eddies with different length scales and in constant interaction with each other.

Turbulence modeling closes the Navier-Stokes equations which govern the behavior of turbulent flows. For incompressible flows, the averaged continuity and momentum equations are described by the following expressions in tensor notation (Ferziger and Peric, 2002):

$$\frac{\partial(\rho\bar{u}_i)}{\partial x_i} = 0 \tag{9}$$

$$\frac{\partial(\rho\bar{u}_i)}{\partial t} + \frac{\partial}{\partial x_j}\left(\rho\bar{u}_i\bar{u}_j + \rho\overline{u'_iu'_j}\right) = -\frac{\partial\bar{p}}{\partial x_i} + \frac{\partial\bar{\tau}_{ij}}{\partial x_j} \tag{10}$$

Where ρ is the density, $\bar{u}_i$ is the averaged Cartesian components of the velocity vector, $\rho\overline{u'_iu'_j}$ is the Reynolds stresses and p is the mean pressure $\bar{\tau}_{ij}$ represents the mean viscous stress tensor components, as follows:

$$\bar{\tau}_{ij} = \mu\left(\frac{\partial\bar{u}_i}{\partial x_j} + \frac{\partial\bar{u}_j}{\partial x_i}\right) \tag{11}$$

In which μ is the dynamic viscosity.

2.5.1. Reynolds Averaged Navier – Stokes (RANS) Models

The need of simulating all scales of turbulence is removed by using a time averaging process. These models use one length scale to characterize the entire turbulent spectrum. Within the RANS models we find:
- Spalart – Allmaras
- K – Epsilon *(k – ε)*
- K – Omega *(k – ω)*
- Reynolds Stress Transport

2.5.1.1. Spalart – Allmaras

This is a one equation model solving a transport equation for a variable called the Spalart-Allmaras variable, which is used to define the turbulent eddy viscosity. This model is simple, economical and robust when used on good meshes. Its drawbacks are the poor prediction of separation and the impossibility to be used for some combustion models.

2.5.1.2. K – Epsilon (*k – ε*)

This is a two equation model that includes two extra transport equations to represent the turbulent properties of the flow. One of the transport equations is defined for the turbulent kinetic energy, *k*, and the other equation is for the turbulent dissipation, *ε*. This model is insensitive to inflow conditions but its accuracy is poor when simulating many problems, including those with swirl and separation.

2.5.1.3. K – Omega (*k – ω*)

This is a two equation model that includes two extra transport equations to represent the turbulent properties of the flow. One of the transport equations is defined for the turbulent kinetic energy, *k*, and the other equation is for the specific dissipation, *ω*. Two well known variants of this model are the standard and the Shear Stress Transport (SST).

The standard $k - \omega$ model has some advantages that include its good performance for swirling flows and for adverse pressure gradients, but its disadvantage lies in the sensitivity to inlet/freestream turbulence boundary conditions. The SST model was formulated to obtain good predictions near the wall and in the bulk flow to avoid sensitivity to freestream conditions. The basic formulation for the $k - \omega$ model is as follows:

$$\frac{\partial k}{\partial t} + V_j \frac{\partial k}{\partial x_j} = P_k - \beta^* k\omega + \frac{\partial}{\partial x_j}\left[(v + \sigma_k v_T)\frac{\partial k}{\partial x_j}\right] \tag{12}$$

$$\frac{\partial \omega}{\partial t} + V_j \frac{\partial \omega}{\partial x_j} = \alpha S^2 - \beta\omega^2 + \frac{\partial}{\partial x_j}\left[(v + \sigma_\omega v_T)\frac{\partial \omega}{\partial x_j}\right] + 2(1 - F_1)\sigma_{\omega2}\frac{1}{\omega}\frac{\partial k}{\partial x_i}\frac{\partial \omega}{\partial x_i} \tag{13}$$

where v_T is the turbulent eddy viscosity and V_j, x_i and x_j are components of the velocity and position, respectively.

2.5.1.4. Reynolds Stress Transport

This is a seven equation model that uses six equations to resolve Reynolds stresses and one equation for the turbulent dissipation. This model is the most complete and complex of the RANS models and, among its advantages, it is well known for capturing anisotropy (in swirling flows, for example). Among the downsides of the model are that it is computationally expensive and requires high quality meshes.

3   METHODOLOGY

3.1   CFD Approach

The way to obtain coatings with different roughnesses is explained in detail in Savio et al. (2015). The coating applications were made by spraying the surfaces to give the three levels of roughness A, B and C. Level A of roughness simulates an optimal newly built ship or full blast dry docking paint application. The second level (B) of roughness represents a poorly applied coating, and roughness C represents a severe case of underlying roughness accumulated from many dry dockings and a very poor application.

The plates were scanned afterwards by a 3D laser profilometer, which gave data files with coordinates XYZ that reproduce the irregularities of the different surfaces. Figure 5 shows an example of the surface visualized in MATLAB that resulted from the scanning process.
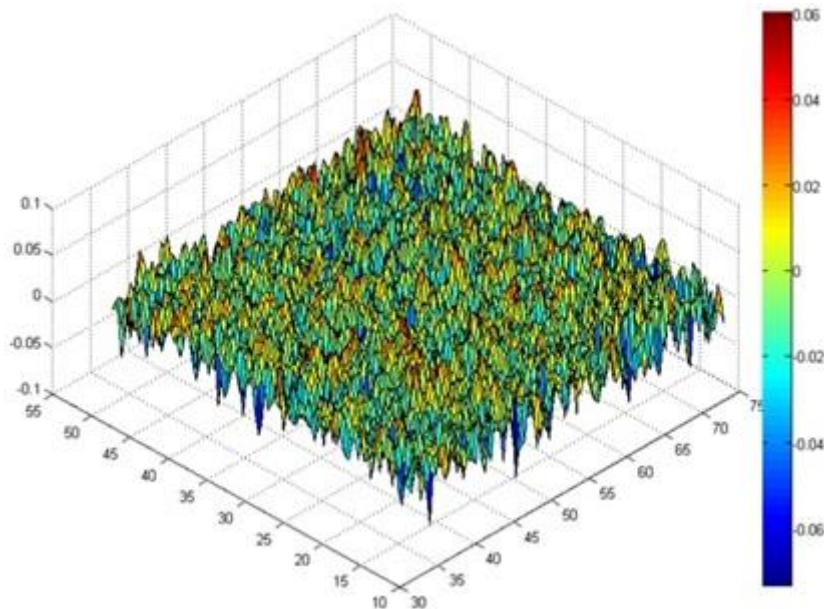

Fig. 5. Surface with roughness level A. Dimensions in mm.

Since use of the entire scanned area for simulation implies expensive computational resources, a representative area of the entire scan was selected for simulation (5 mm × 20 mm). This simulated area should exhibit characteristics of the roughness present in the entire plate. This representative area is then transformed into an STL file that can be read by the meshing software in which the domain is created that is then solved by the CFD solver.

The software used for creating the meshes was ICEM CFD V.17. The STL files were imported into this software to create open channel meshed domains with a height of 0.02 m. The number of cells for the different cases varied between 5 and 6 million. All meshes were refined near the bottom wall of the domain, and a mesh dependency test was carried out by evaluating how the wall shear stress varied when the number of cells increased.
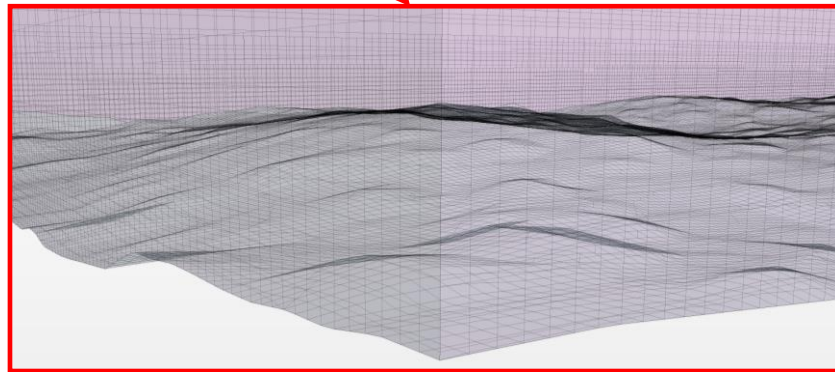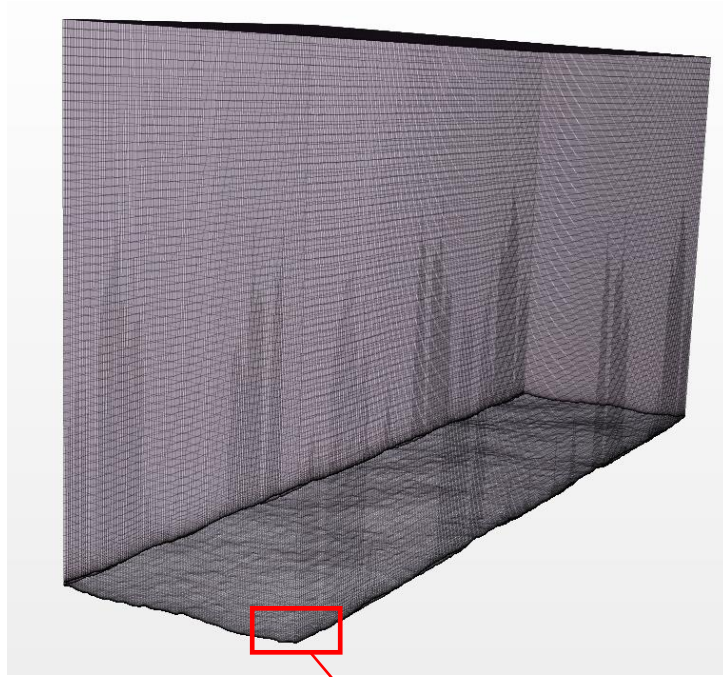
Fig. 6. Meshed domain for case B with a zoomed area close to the bottom wall.

The bottom of the domain (where the roughness is present) was set as a no-slip boundary, whereas the top is a symmetry wall. For the inlet and outlet boundaries, periodic boundary conditions were set and the mass flow was specified, which corresponded to Reynolds numbers 84000 to 280000.

The physical model used in the computations is as follows:
- Steady flow
- Segregated flow
- Reynolds-Average Navier Stokes (RANS)
- $k -$ omega turbulence model, Shear Stress Transport (SST)
- All y^+ wall treatment

The simulations are considered converged when the values of the wall shear stress acting on the bottom surface of the domain shows an asymptotic behavior and the difference in values of the wall shear stress between the last and previous iteration is at least 0.1%. The plots for residuals are also monitored to confirm convergence.

In order to calculate the friction velocity, the total pressure and viscous force acting on the rough wall caused by the flow are considered. It is possible to invoke a force report in Star CCM+ to calculate the total pressure and shear forces in the region or surface of interest. The complete procedure of the CFD approach is explained in more detail in Niebles Atencio and Chernoray (2016).

3.2   Experiments

A rotating disk rig was designed and constructed for Micro-PIV and torque measurements. The disk is driven by an electric motor and rotates inside a 20-liter tank filled with water at a temperature around 20°C. A schematic of the rig is shown in Fig. 7.
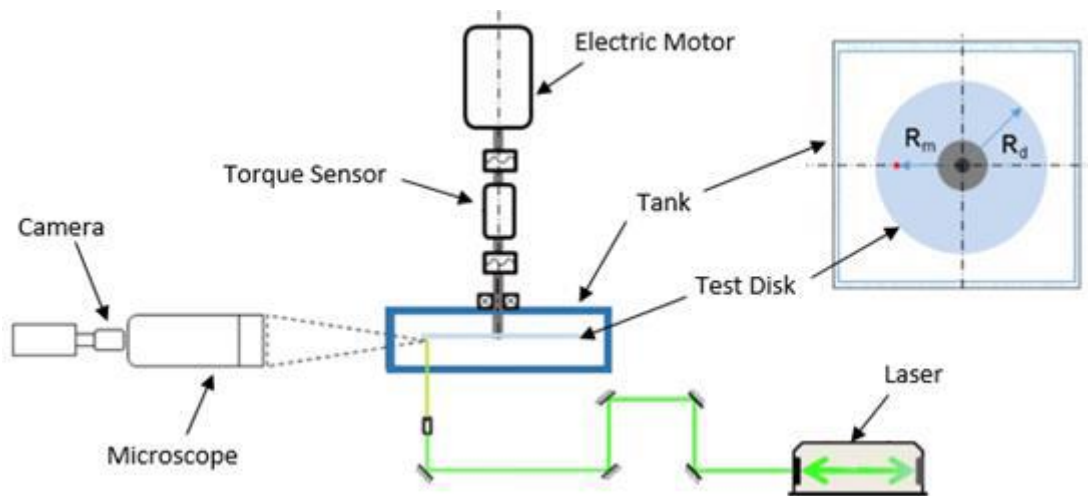

Fig. 7. Schematic of the rotating disk rig.

Different disks with different roughnesses were used for the experiments. These include one smooth disk for reference, two cases with sandpaper, three cases of disks with different antifouling painting applications (corresponding to roughnesses A, B and C explained in section 3.1) and one case with periodic roughness. Table 1 illustrates the different cases and their average roughness. The peak value of roughness is given for the periodic roughness.
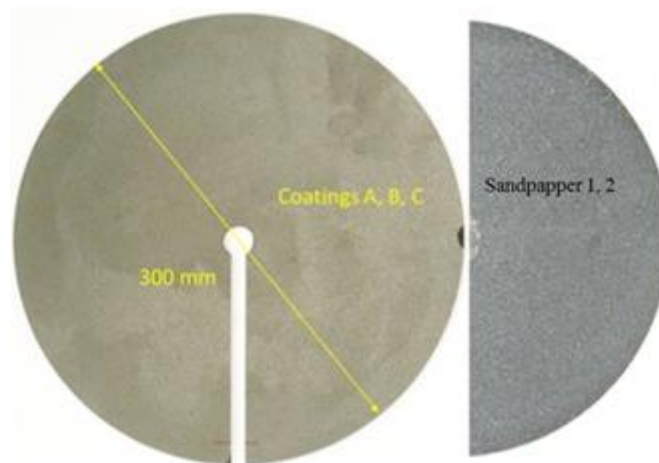

Fig. 8. Disks used for experiments in the rotating disk rig.

Table 1. Experimental cases of surface roughness for the rotating disks with their average heights in micrometers.

Smooth	A	B	C	80-G	400-G	Periodic
0.55	13	33	55	201	35	500 (peak)

3.2.1. MicroPIV Measurements in Rough-Wall Boundary Layers

Measurement of boundary layer profiles on disks is a challenging task due to the very small thickness of the boundary layer (3–5 mm). To measure the azimuthal velocity component near the disk wall with the high spatial resolution and to capture the inner layer of the turbulent boundary layer, a microscopic optics was used with a magnification of 12 times.

The seeding of the flow was done by using PMMA microparticles GmbH of 1 µm in diameter. The images were registered, magnified and transferred by a monochrome double-frame CCD camera with a resolution of 2048×2048 pixels^2. The recording of this camera was synchronized with the specific angle of rotation of the test disk through a hall sensor. Complete details and the set-up for these measurements are described in Niebles Atencio, Tokarev and Chernoray (2016).

3.2.2. Torque Measurement Tests

For the torque measurement test, a Kistler type 4503A torque meter was installed on the rotating disk rig connecting the electric motor and the rotating disk shaft (as shown in Fig. 7). The torque sensor operates based on the strain gauge principle. The torque meter output was monitored by an analogue to digital converter (ADC) controlled by a PC. The torque was measured for rotational velocities from 0 to 1200 rpm. The measurement procedure included a warm up of the running rig and the measurement equipment for at least one hour before experiments.

3.2.3. Towing Tank Tests

Towing tank tests were performed by the Norwegian Marine Technology Research Institute (MARINTEK) and reported by Savio et al. (2015). In summary, test plates with different roughnesses A, B and C (previously mentioned in section 2) were towed in the wake of a leading (front) plate which was smooth. The Reynolds numbers during tests were based on the total length of plates and ranged between 3×10^7 and 9×10^7.

4   RESULTS

4.1   Micro-PIV measurements

Figure 9 shows dimensionless velocity profiles for the different cases obtained from PIV. Cases that were smooth and had roughnesses A, B and C are also compared with resolved CFD computations. As can be seen, the velocity profiles between experiments and CFD agree (or at least are close) for the smooth and rough case A, that is, for the smallest roughness cases. As the roughness increases, the difference between the CFD and the experiments is more noticeable. The experiments show that the dimensionless velocity profiles move downwards to a greater degree as the roughness increases, which is the expected behavior. This downwards displacement of the velocity profile in the rough cases with respect to the smooth case is known as the roughness function, ΔU^+.
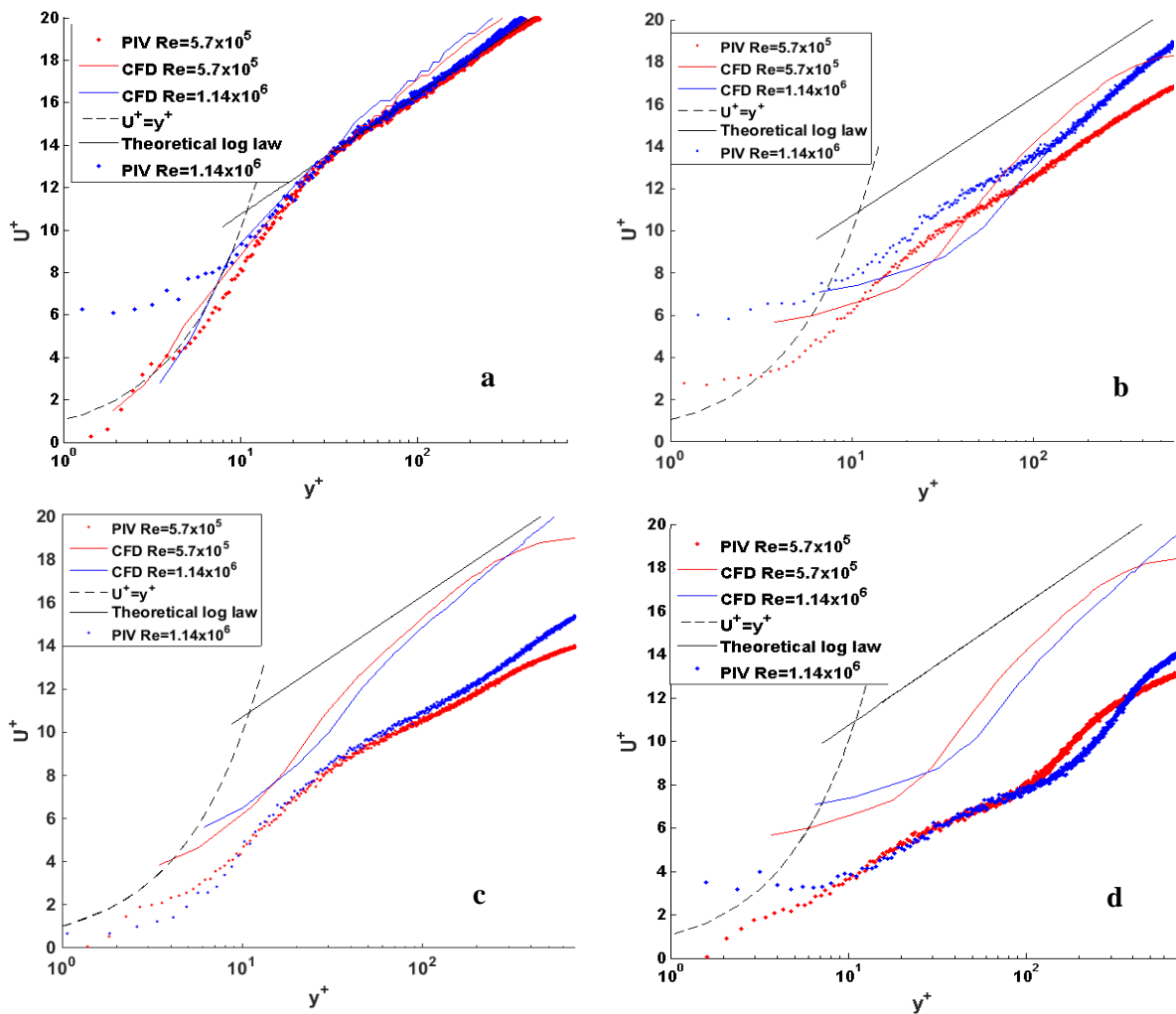

Fig. 9. Dimensionless velocity profiles from micro-PIV measurements compared with resolved CFD simulations (a: smooth case; b: roughness case A; c: roughness case B; d: roughness case C)

A velocity profile from one of the 80-G sand-paper case is shown in Fig. 10, compared with the theoretical profile. The micro-PIV measurements can also capture the velocity decrement caused by the presence of roughness.
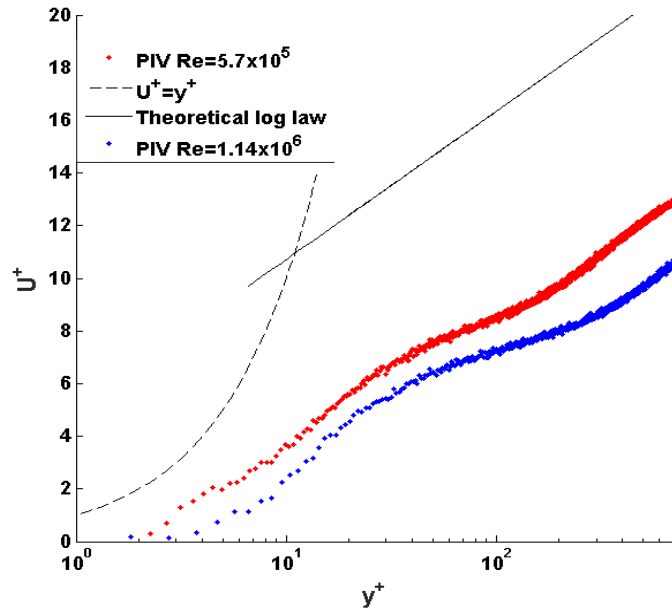
Fig. 10. Velocity profile from micro-PIV for one of the sand-paper cases

4.2 Torque Measurements, Towing Tank Tests and resolved CFD

Figures 11, 12 and 13 show results after post-processing the torque measurements, the data from the towed plates and the resolved CFD simulations. This post-processing was done according to Granville (1987). What is presented in the plots is how the resistance caused by the roughness varies with the Reynolds number. The Reynolds numbers are defined differently, depending on the case. Only results for antifouling paints are analyzed (i.e., cases A, B and C). From these plots we can indirectly obtain the velocity decrement (ΔU^+) and, once it is determined, we are able to compare the resulting ΔU^+ in the three cases (Fig. 14).
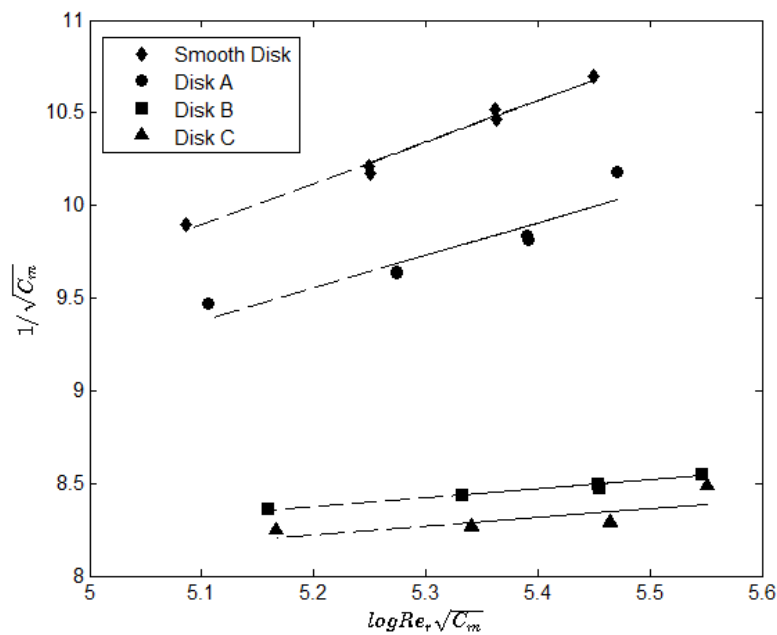

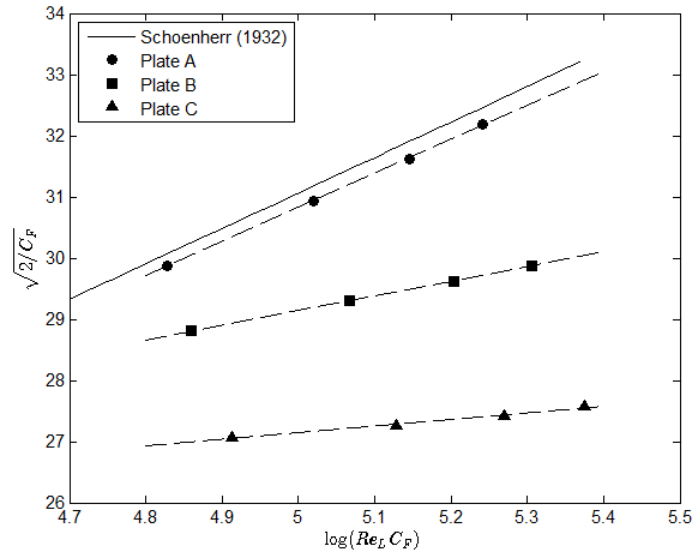Fig. 11. Post-processing of torque measurement tests.
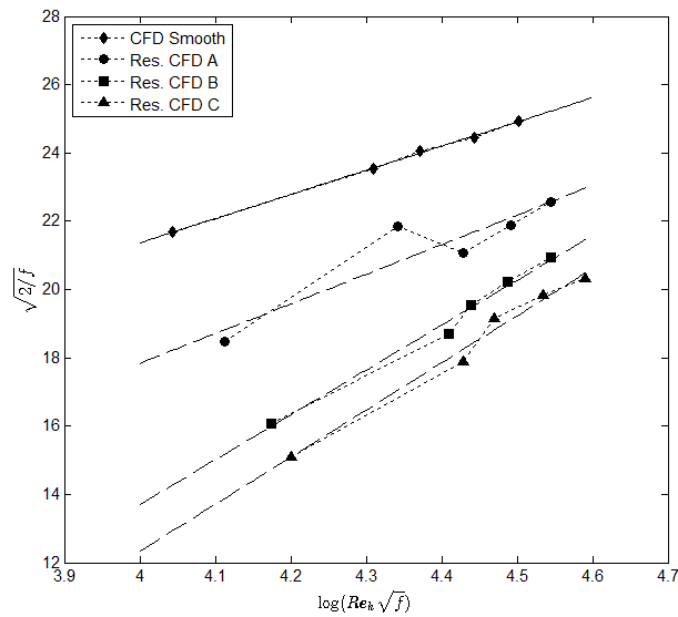
Fig. 12. Towing tank tests results

Fig. 13. Results from the resolved CFD simulations.

ΔU^+ values obtained from the previously presented plots are shown in Fig. 14 against the roughness Reynolds number according to the definition given by equation (3). In this case, the roughness height is the root mean square of roughness (R_q) for cases A and B, while the equivalent roughness height of 43 μm is used for case C. The Cebeci and Bradshaw (1977) roughness function is also shown using two different values for the roughness constant, C_s. Looking at the figure, it seems that, for the towed plates, the resulting drag in case A is caused by a smaller roughness than the A case roughness for rotating disk and resolved CFD. If we follow the same reasoning, the roughness for plate B seems to be similar to the roughness of A of the resolved CFD. Plate C seems to match case C for the CFD cases.

Regarding the rotating disk cases, similar results are clearly seen for case B, when compared with the CFD, but case A seems to be smoother than its counterpart in the CFD simulations.

The CFD simulations generally show good agreement with experiments, but the results might be over predicted for the case of roughness A.

The results show that the roughness function by Cebeci and Bradshaw with $C_s = 0.5$ describes the data at a high Reynolds number, using R_q as the roughness height. For cases B and C, similar results are seen when comparing the resolved CFD simulations and the experiments.
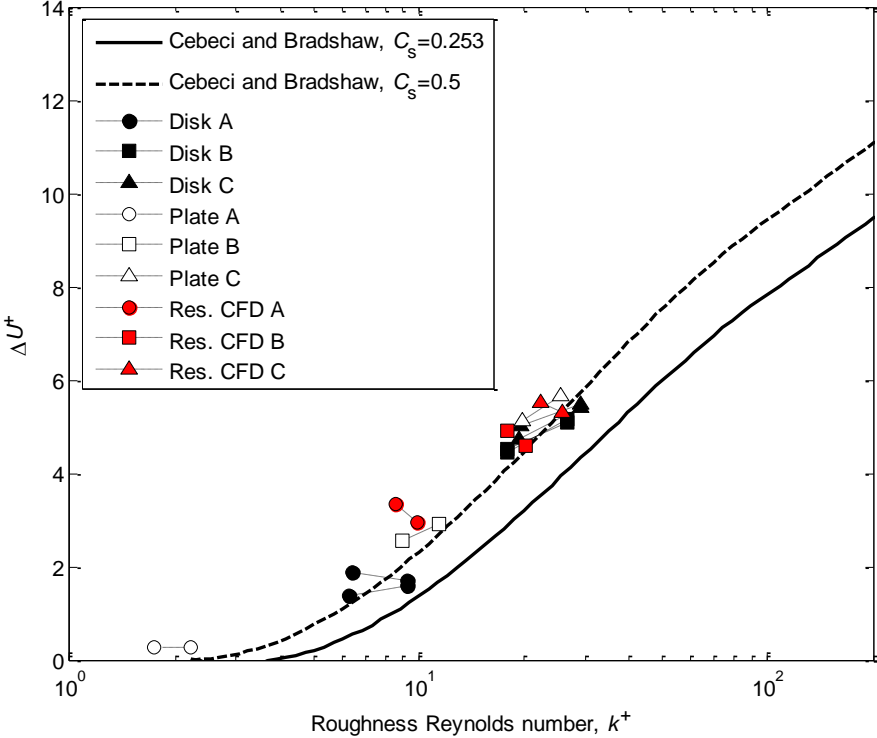

Fig. 14. Comparison of results from torque, towed plates and resolved CFD.

5   CONCLUDING REMARKS AND FUTURE WORK

Studies to identify the effect of different rough surfaces on the velocity profiles were carried out in experiments and resolved CFD. The tests were done in a rotating disk rig using long-distance micro-PIV and torque measurements.

A drag evaluation of antifouling paints was made by using indirect methods that could validate a newly developed approach based on resolved RANS simulations. This new CFD based approach is useful because we can replace expensive experiments and find, with acceptable reliability, the roughness function of arbitrary roughness.

Simulating the effects of realistic rough surfaces by resolved CFD is quite challenging; therefore, improving the accuracy of predictions is one task to be addressed in the future.

The wall determination in micro-PIV experiments is quite important and critical for the correct location of the velocity profiles. With this information, we can match experiments and CFD computations.

The next step would be comparing the drag evaluation method with more experiments (improved micro-PIV measurements) and using realistic fouled surfaces.

The small scale rig has shown itself to be a very practical and compact way to estimate the drag caused by rough surfaces and can be used to replace more expensive large scale tests.

6 REFERENCES

Allen J.J, Shockling M.A, Smits A.J. 2005 Evaluation of a universal transition resistance diagram for pipes with honed surfaces. Phys. Fluids. 17, 121 702–121 706.

Anderson, C., Atlar, M., Callow, M., Candries, M., Milne, A., Townsin, R. 2003. The development of foul-release coatings for seagoing vessels. J. of Marine Design and Operations, No. B4, 11–23.

Ashrafian, A., Andersson, H. and Manhart, M. 2004. DNS of turbulent flow in a rod-roughened channel. Int. J. Heat Fluid Flow 25, 373–383.

Bhaganagar, K., Kim, J. and Coleman, G. 2004. Effect of roughness on wall-bounded turbulence. Flow, Turbulence and Combustion 72: 463–492.

Candries, M. and Atlar, M. 2003. Estimating the impact of new generation antifoulings on ship performance: the presence of slime. J. of Marine Eng. and Technology 2, 13–22.

Cebeci, T. and Bradshaw, P. 1977. Momentum Transfer in Boundary Layers, Hemisphere Publishing/McGraw-Hill, 176–180.

Clauser, F. H., 1954. Turbulent boundary layers in adverse pressure gradients, J. Aerosol Sci. 21, 91–108.

Colebrook, C. F., 1939. Turbulent flow in pipes, with particular reference to transitional region between smooth and rough wall laws, J. Ins. Civ. Eng. 11, 133–156.

Demirel, Y., Khorasanchi, M., Turan, O. and Incecik, A. 2014a. A CFD model for the frictional resistance prediction of antifouling coatings. J. Ocean Eng. 89, 21–31.

Demirel, Y., Khorasanchi, M., Turan, O. and Incecik, A. 2014b. CFD approach to resistance prediction as a function roughness. Proc. of Transp. Research Arena Conf. 2014.

Flack, K. A., Schultz, M. P. and Shapiro, T. A. 2005. Experimental support for Townsend's Reynolds number similarity hypothesis on rough walls. Phys. Fluids 17, 035102.

Flack, K. and Schultz, M., 2010. Review of Hydraulic Roughness Scales in the Fully Rough Regime. J Fluid Eng. 132, 1–9.

Flack, K. and Schultz, M. 2014. Roughness effects on wall-bounded turbulent flows. Phys. Fluids 26, 1013051-10130516.

George, W., 2007. Is there a universal log law for turbulent wall-bounded flows? Phil. Trans. R. Soc. A 365, 789–806.

Granville P.S. 1982. Drag-characterization method for arbitrarily rough surfaces by means of rotating disks. J. Fluids Eng. 104, 373–377.

Granville P.S. 1987. Three indirect methods for the drag characterization of arbitrarily rough surfaces on flat plates. J. Ship Res. 31, 70–77.

Grigson, C.W. 1992. Drag losses for new ships caused by hull finish. J. Ship. Res. 36, 182–196.

Hama F. R., 1954. Boundary-layer characteristics for rough and smooth surfaces, Trans. SNAME 62, 333–351.

ITTC 1978. Performance prediction method. International Towing Tank Conference, 1978.
ITTC 2005. Report of the powering performance committee. International Towing Tank Conference, 2005.

Jimenez, J. 2004. Turbulent flows over rough walls. Ann. Rev. Fluid Mech. 36, 173–196.

Khor, Y.S. and Xiao, Q. 2011. CFD simulations of the effects of fouling and antifouling. Ocean Eng. 38, 1065–1079.

Krogstad, P.A. and Efros, V. 2012. About turbulence statistics in the outer part of a boundary layer developing over 2D surface roughness. Phys. Fluids 24, 075112.

Kunkel, G. and Marusic, I., 2006. Study of the near-wall turbulent region of the high Reynolds-number boundary layer using an atmospheric flow. J. Fluid Mech. 548, 375–402.

Langelandsvik, L., Kunkel, G. and Smits, A. 2008. Flow in a commercial steel pipe. J. Fluid Mech. 595, 323–339.

Lee, J. H., Sung, H. J. and Krogstad, P. 2011. Direct numerical simulation of the turbulent boundary layer over a cube-roughened wall. J. Fluid Mech. 669, 397–431.

Leonardi, S., Orlandi, P., Smalley, R., Djenidi, L. and Antonia, R., 2003. Direct numerical simulations of turbulent channel with transverse square bar on one wall. J. Fluid Mech. 491, 229–238.

Moody, L. F., 1944. Friction factors for pipe flow. Trans. ASME 66, 671–688.

Nikuradse, J. 1933. Laws of flow in rough pipes, NACA Technical Memorandum 1292.

Österlund, J. M., Johansson, A. V., Nagib, H. M. and Hites, M. H. 2000. A note on the overlap region in turbulent boundary layers. Phys. Fluids 12, 1–4.

Raupach, M., Antonia, R.A. and Rajagopalan, S., 1991. Rough-wall turbulent boundary layers. Appl. Mech. Rev. 44, 1 –25.

Savio, L., Ola Berge, B., Koushan, K. and Axelsson, M. 2015. Measurements of added resistance due to increased roughness on flat plates. In Proc. of 4th Int. Conf. on Advanced Model Measurement Technology for the Maritime Industry (AMT'15).

Schlichting, H. 1979a. Boundary Layer Theory, McGraw-Hill, New York, 616–617.

Schlichting, H. 1979b. Boundary Layer Theory, McGraw-Hill, New York, 647

Taylan, M. 2010. An overview: Effect of roughness and coatings on ship resistance, In Proc. of Int. Conf. on Ship Drag Reduction, SMOOTH-SHIPS.

Townsin, R., Byrne, D., Svensen, T. and Milne, A. 1981. Estimating the technical and economic penalties of hull and propeller roughness. Trans. SNAME 89, 295–318.

UNCTAD 2015. Review of Maritime Transport. United Nations Conference on Trade and Development (UNCTAD).

Yuan, J. and Piomelli, U. 2014. Estimation and prediction of the roughness function on realistic surfaces. J. Turbulence 15, 350–365.

Zanoun, E.-S., Durst, F. and Nagib, H. 2003. Evaluating the law of the wall in two-dimensional fully developed turbulent channel flows. Phys. Fluids 15, 3079–3089.

APPENDED PAPERS